

# Phase Field Benchmark Problems for Nucleation

W. Wu<sup>a,b</sup>, D. Montiel<sup>c</sup>, J. E. Guyer<sup>d</sup>, P. W. Voorhees<sup>a,f</sup>, J. A. Warren<sup>d</sup>, D. Wheeler<sup>d</sup>,  
L. Gránásy<sup>g</sup>, T. Pusztai<sup>g</sup>, O. G. Heinonen<sup>b,e</sup>

<sup>a</sup>*Center for Hierarchical Materials Design, Northwestern University, 2205 Tech Drive, Suite 1160,  
Evanston, IL, 60208, USA*

<sup>b</sup>*Materials Science Division, Argonne National Laboratory, 9700 South Cass Avenue, Lemont, IL 60439,  
USA*

<sup>c</sup>*Department of Materials Science and Engineering, University of Michigan, 2300 Hayward Street, Ann  
Arbor, MI, 48109, USA*

<sup>d</sup>*Material Measurement Laboratory, National Institute of Standards and Technology, 100 Bureau Drive, MS  
8300, Gaithersburg, MD 20899-8300, USA*

<sup>e</sup>*Northwestern-Argonne Institute of Science and Engineering, 2205 Tech Drive, Suite 1160, Evanston,  
Illinois 60208, USA*

<sup>f</sup>*Department of Materials Science and Engineering, Northwestern University, 2220 Campus Drive,  
Evanston, IL 60208, USA*

<sup>g</sup>*Department of Experimental Solid State Physics, Institute for Solid State Physics and Optics, Wigner  
Research Centre for Physics, 29-33, Konkoly-Thege Miklós út, Budapest, Hungary, H-1121*

---

## Abstract

We present nucleation phase field model benchmark problems, expanding on our previous benchmark problems on diffusion, precipitation, dendritic growth, linear elasticity, fluid flow and electrochemistry. Nucleation is the process in which either a new thermodynamic phase or a new structure is created, such as solidification from the melt, or self-assembly of particulates. Based on where the nucleation occurs, it can be divided into two main categories: homogeneous nucleation and heterogeneous nucleation. In the first nucleation benchmark problem, we focus on homogeneous nucleation for both single seed under different initial conditions and multiple seeds. The second nucleation benchmark problem focuses on athermal heterogeneous nucleation and nucleation behavior near the free growth limit with different undercooling driving forces.

*Keywords:* phase field, benchmark, nucleation

---

## 1. Introduction

We continue our series of Benchmark Problems for Phase Field models. They are developed by the Center for Hierarchical Materials Design (CHiMaD) and the National Institute of Standards and Technology (NIST) together with considerable support from the phase field community of developers and modelers. The purpose of the benchmark problems is to

---

*Email addresses:* wuw@anl.gov (W. Wu), dmontiel@umich.edu (D. Montiel), guyer@nist.gov (J. E. Guyer), p-voorhees@northwestern.edu (P. W. Voorhees), james.warren@nist.gov (J. A. Warren), daniel.wheeler@nist.gov (D. Wheeler), granasy.laszlo@wigner.mta.hu (L. Gránásy), pusztai.tamas@wigner.mta.hu (T. Pusztai), heinonen@anl.gov (O. G. Heinonen)

provide resources to test new algorithms and codes for numerical accuracy, and to train new researchers. In the publication series of the phase field benchmark problems we present the rationale for selecting and defining the problems, suggest metrics for testing and comparing solutions, and also present sample solutions. The problems are selected from the canon of phase field modeling, and often include multi-physics couplings that may be encountered in typical problems and that may frustrate numerical solutions. Previous problems focused on diffusion of solute and second phase coarsening [1], solidification of an undercooled liquid (dendritic growth) and linear elasticity [2], and Stokes flow and electrostatics [3]. Solidification, in particular, is of enormous practical and theoretical importance for various branches of science, including physical chemistry, materials science, biophysics, geophysics, and cryobiology, to name a few. Previous work introduced a benchmark problem for dendritic growth describing complex solidification patterns in an undercooled liquid or solution [2]. This work introduces a benchmark for nucleation which models the initial stages of the solidification process and, thus, complements the solidification benchmark, which models the later stages of solidification. It is of interest to extend the phase field Benchmark Problems to nucleation, as it is a process that sets the initial microstructure for solidification, growth, and coarsening. Phase field modeling of nucleation has a long history and is also covered in a number of reviews [4, 5, 6, 7, 8, 9, 10]. The problem formulation of crystallization of an ideal pure liquid cooled below its melting point starts with homogeneous nucleation, a process in which the internal fluctuations of the undercooled liquid lead to the formation of crystal-like seeds able to grow to macroscopic sizes. The nucleation can be assisted by the presence of surfaces (container walls, foreign particles, etc.), in which case the process is termed heterogeneous nucleation. We note that homogeneous nucleation is an idealized formulation, and it is unlikely homogeneous nucleation occurs, due to impurities present in experimental apparatus. However, creating benchmark problems for homogeneous nucleation is still needed since the focus in nucleation research often lies on the underlying homogeneous nucleation, as it is the basis for advancing theoretical approaches to the much more complex phenomena governing heterogeneous nucleation.

We present two Benchmark Problems on nucleation, with the first one targeting homogeneous nucleation. There are two main modeling approaches to introduce nuclei into a metastable system: the Langevin noise method [11, 4] and the explicit nucleation method [12, 13]. We focus on the explicit method, where the critical nucleus size and the nucleation energy are determined by the classical nucleation theory. In contrast with the Langevin noise method, the explicit nucleation method allows for consideration of nucleation events that may occur whenever there is a sufficient driving force. We break down our consideration of homogeneous nucleation into three parts. The first part considers the simple case of single-seed homogeneous nucleation. We explore how the particle size influences the evolution of the nucleus when the thermodynamic driving force is close to the critical value where we can observe whether the particle grows, dissolves or remains stationary. In the second and third parts we consider multiple-seeds homogeneous nucleation, with nuclei appearing at fixed time  $t = 0$  or at random times distributed uniformly, respectively, with the latter part illustrating a scenario with constant nucleation rate. The Benchmark Problem probes the differences between transformation kinetics of the two cases and summarizes them using the Avrami plots based on the Johnson-Mehl-Avrami-Kolmogorov (JMAK) theory [14, 15, 16, 17, 18]. The second Benchmark Problem focuses on athermal heterogeneous nucleation as proposed

by Quested and Greer [19]. Athermal nucleation can explain the performance of inoculants in grain-refining of commercial aluminum alloys [20, 21]. The particles remain dormant at and below a critical undercooling, at which the radius of the particles is equal to that of the critical radius for the homogeneous nucleus. Further free growth is possible if the degree of undercooling is increased. The Benchmark Problem explores the nucleation behavior around the free growth limit with different undercooling driving forces. [We use a simple example for the heterogeneous nucleation. In more complex realistic scenarios, the phase field method could remove some of the critical assumptions involved in classical approaches to heterogeneous nucleation existing in the literature and predict significantly different critical nuclei shapes and activation energy barriers \[22, 23\].](#)

The mathematical and algorithmic implementation of these Benchmark Problems is relatively simple compared to other Benchmark Problems, e.g., the coupled Cahn-Hilliard-linear elastic problem, or the coupled Cahn-Hilliard-Poisson Benchmark Problem [2, 3]. However, this does not make solving the problems numerically trivial, and we deliberately chose undercoolings in some problem formulations that stress convergence of the solver. Nevertheless, the solutions should be relatively straightforward, and we believe that the pedagogical aspect of introducing nucleation Benchmark Problems is an important one. As with the previous Benchmark Problems, we present suggested metrics for how to evaluate solutions for the nucleation benchmark problem. In addition to our own solutions presented here, The PFHub website [24] (<https://pages.nist.gov/pfhub/>) hosts our solutions as well as solutions by others using a variety of codes. We encourage readers to upload their solutions and to explore the additional resources there, and to participate in discussions around the Benchmark Problems.

## 2. Model formulations

### 2.1. The phase field model in classical nucleation theory

For these benchmark problems we use the simplest possible phase field model with a single non-conserved phase field  $\phi$ , which describes an isothermal pure substance with one liquid ( $\phi = 0$ ) and one solid ( $\phi = 1$ ) phase. The free energy of this system is

$$\mathcal{F}(\phi) = \int \left[ \frac{\epsilon^2}{2} (\nabla\phi)^2 + wg(\phi) - \Delta fp(\phi) \right] dV, \quad (1)$$

set  $g(\phi) = \phi^2(1 - \phi)^2$ , a simple double well function with minima at  $\phi = 0$  and  $\phi = 1$ ,  $w$  controls the double-well barrier height,  $\epsilon^2$  is the gradient energy coefficient, let  $p(\phi) = \phi^3(10 - 15\phi + 6\phi^2)$ , which ensures that  $p(0) = p'(0) = p'(1) = 0$  and  $p(1) = 1$ , and  $\Delta f$  is the driving force for solidification at the simulation temperature ( $\Delta f$  is positive below the melting point). The time evolution of  $\phi$  is given by the Allen-Cahn equation [25]

$$\frac{\partial\phi}{\partial t} = -M \frac{\delta\mathcal{F}}{\delta\phi} = M [\epsilon^2 \nabla^2 \phi - wg'(\phi) + \Delta fp'(\phi)] \quad (2)$$

where  $M$  is the mobility parameter. We will restrict the problem to two dimensions (2D). For a planar interface, one can show that the equilibrium ( $\Delta f=0$ ) solid-liquid interface profile

with the interface centered at  $x = x_0$  is given by

$$\phi(x) = \frac{1}{2} \left[ 1 - \tanh \left( \frac{x - x_0}{\sqrt{2}\ell} \right) \right], \quad (3)$$

where  $x$  is the perpendicular distance from the interface. We use this expression as the initial condition when we introduce a nucleus. We can also obtain the width  $\ell$  and the free energy of the interface,  $\gamma$ , as

$$\ell = \sqrt{\frac{\epsilon^2}{w}} \quad (4)$$

and

$$\gamma = \frac{\sqrt{\epsilon^2 w}}{3\sqrt{2}}. \quad (5)$$

Choosing a characteristic length scale  $\xi = \ell$  and a characteristic time scale  $\tau = 1/(Mw)$ , we can obtain a nondimensional form of the problem (the nondimensional quantities are denoted by tildes),

$$\tilde{\mathcal{F}}(\phi) = \int \left[ \frac{1}{2}(\tilde{\nabla}\phi)^2 + g(\phi) - \tilde{\Delta}fp(\phi) \right] d\tilde{V} \quad (6)$$

and

$$\frac{\partial\phi}{\partial\tilde{t}} = \tilde{\nabla}^2\phi - g'(\phi) + \tilde{\Delta}fp'(\phi), \quad (7)$$

with  $\tilde{\Delta}f = \Delta f/w$ .

## 2.2. The properties of the classical nucleus

The explicit nucleation method that we employ introduces nuclei into a metastable system, with their radii and nucleation barrier determined from classical nucleation theory. Classical nucleation theory views crystallite fluctuations appearing in the undercooled liquid as small spherical domains of the bulk crystalline phase bounded by a mathematically sharp solid-liquid interface. For a 2D system, the free energy of a circular solid particle of radius  $r$  is

$$\Delta G(r) = 2\pi r\gamma - \pi r^2\Delta f \quad (8)$$

where  $\Delta f$  is the nucleation driving force that is used in our phase field model, and  $\gamma$  is the free energy of the interface. The free energy of the particle is a balance between the energy cost in forming the solid-liquid interface, and the free energy from the driving force which is released when the crystalline particle forms. Once the rate of change of free energy with respect to particle size becomes negative, the particle can grow. Taking the derivative of  $\Delta G(r)$  we get the rate of change of free energy with respect to radius as

$$\frac{d\Delta G}{dr} = 2\pi\gamma - 2\pi r\Delta f. \quad (9)$$

By setting  $d\Delta G/dr$  to zero, we obtain the critical radius  $r^*$  as

$$r^* = \frac{\gamma}{\Delta f}. \quad (10)$$

The corresponding critical nucleation free energy is

$$\Delta G^* = \frac{\pi\gamma^2}{\Delta f}. \quad (11)$$

Using the same units as before, the nondimensional forms of these quantities are

$$\tilde{r}^* = \frac{1}{3\sqrt{2}} \frac{1}{\tilde{\Delta f}} \quad (12)$$

and

$$\Delta \tilde{G}^* = \frac{\pi}{18} \frac{1}{\tilde{\Delta f}}, \quad (13)$$

respectively.

### 2.3. Avrami plots

Avrami plots describe how solids transform from one phase to another at constant temperature. In particular, they can describe the kinetics of nucleation. The Avrami plots come from the JMAK theory [14, 15, 16, 17, 18], which makes a number of assumptions and simplifications: (i) nucleation occurs randomly and homogeneously over the entire un-transformed portion of the material, (ii) the growth rate is constant and does not depend on the extent of transformation, (iii) the particles have convex shape with the same orientation, and (iv) the size of the system is infinite and so is the time period in which the transformation occurs.

The basis of the Avrami plots is the transformed fraction (solid fraction)  $Y(t)$  vs. time. According to the JMAK theory,

$$Y(t) = 1 - \exp(-Kt^n), \quad (14)$$

where  $K$  is a constant depending on the nucleation and growth rates,  $n = d+1$  for continuous nucleation and  $n = d$  if nucleation happens only at  $t = 0$ , and  $d$  is the number of spatial dimensions. If we plot  $\ln[-\ln(1 - Y(t))]$  vs.  $\ln(t)$ , then for the JMAK kinetics (Eq. 14) we get a straight line with slope  $n$ .

## 3. Nucleation benchmark problems

We present two nucleation benchmark problems in this set of benchmarks, the first for homogeneous nucleation and the second for athermal heterogeneous nucleation. From here on, we will use only the nondimensional forms of the phase field (Eqs. 6, 7, and 3) and nucleation (Eqs. 12 and 13) equations, but we will drop the tildes.

### 3.1. Problem I.1 – Homogeneous nucleation, single seed

In this problem we examine the morphology change of the nucleus for different initial radii. We consider a 2D simulation domain of size  $100 \times 100$  units centered at  $x = y = 0$  with **zero normal-derivative** Neumann boundary conditions  $\nabla\phi \cdot \hat{n} = 0$  on all boundaries. The driving force is set to  $\Delta f = \sqrt{2}/30$ , which corresponds to a critical radius of  $r^* = 5$  (Eq. 12). ~~Next, we place a circular seed at the center of the domain. Incorporating a nucleus into a diffuse interface phase field model leads to a small offset from a classical,~~

sharp-interface model of a nucleus. To account for this, we incorporate a diffuse-interface seed at the center of the domain using the profile  $\phi(\mathbf{r})$  given by modifying Eq. 3 to 2D where  $\mathbf{r}$  is the vector that starts from the central origin to point  $(x, y)$ . It has been shown that the phase field order parameter profile in a critical nucleus can deviate from that assumed in the classical nucleation theory, especially when the critical radius is close to the interface width [4, 7, 10, 26]. In this problem, we carefully choose the driving force so that the critical radius  $r^* = 5$  is much larger than the interface width  $\ell = 1$ . Therefore, the phase field critical nuclei should behave as described by the classical sharp-interface model. Problem I.1 is then defined by the Allen-Cahn equation

$$\frac{\partial \phi}{\partial t} = \nabla^2 \phi - g'(\phi) + \Delta f p'(\phi) \quad (15)$$

for the phase field  $\phi$ , and the three different initial conditions: in the first case with the seed radius  $r_0$  corresponding exactly to the critical one (critical nucleus), and in the other two cases, slightly below and above the critical radius (subcritical and supercritical nuclei):

$$\phi(\mathbf{r}) = \frac{1}{2} \left[ 1 - \tanh \left( \frac{\|\mathbf{r}\| - r_0}{\sqrt{2}} \right) \right], \quad (16)$$

where  $r_0 = \{r^*, 0.99r^*, 1.01r^*\}$ . We obtain Eq. 16 from Eq. 3 by imposing circular symmetry on the nuclei and use the isotropy of the free energy density. When  $\mathbf{r} = (x, 0)$ , Eq. 16 reduces to the 1D case Eq. 3. Figure 1 shows the computational domain with an initial seed of radius  $r_0 = r^*$ . This seed is the diffuse-interface approximation of the classical sharp interface nucleus corresponding to the given  $\Delta f$ , and therefore it should be fairly close to (an unstable) equilibrium. The time evolution of the system is then followed for times up to  $t = 100$  units, and the solid fraction  $Y$  and the total free energy  $\mathcal{F}$  are plotted as functions of time. Finally, the problem also includes a convergence test with respect to mesh (spatial resolution). The closer the initial radius  $r_0$  is to the critical radius  $r^*$ , the more sensitive the numerical integration will be to round-off errors. Therefore, a convergence check should be performed for  $r_0 = 1.01r^*$  for times up to 200 units. This convergence check can simply be done by halving the average spatial mesh size  $\Delta x$  between consecutive runs until plots of the solid fraction  $Y(t)$  vs. time  $t$  for two consecutive runs become indistinguishable by some measure. For uploads to the PFHub website, the phase field  $\phi$  at the last time step can be uploaded together with the real-space grid points  $(x, y)$  for the mesh used in the simulation. A script on the website can then be used to interpolate solutions on different meshes and calculate a convergence error.

### 3.2. Problem I.2 – Homogeneous nucleation, multiple seeds at $t = 0$

The second part of the homogeneous nucleation benchmark problem focuses on the kinetics of nucleation using Avrami plots and compares them to the JMAK theory. To obtain reasonable statistics for these two parts, the simulation volume needs to be larger so it can encompass a larger number of smaller nuclei. We therefore increase the domain size to  $500 \times 500$  units of length while keeping the same Neumann boundary conditions on all

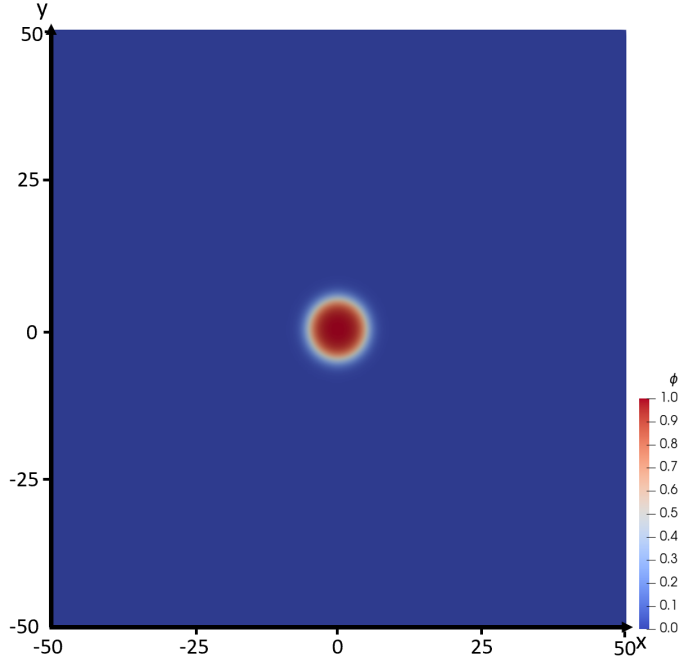


Figure 1: Illustration of the  $100 \times 100$  computational domain in 2D with **zero normal-derivative** Neumann boundary conditions **on all boundaries**. A diffuse-interface circular seed with profile  $\phi(\mathbf{r})$  and radius  $r_0 = r^*$  is placed in the center at  $t = 0$ .

boundaries. We then increase the driving force to  $\Delta f = \sqrt{2}/6$ , which corresponds to a critical radius of  $r^* = 1$ . Random initial positions of 25 supercritical seeds  $\mathbf{r}_1, \dots, \mathbf{r}_{25}$  are generated with  $r_0 = 2.2 = 2.2r^*$  drawn from a uniform distribution on the  $500 \times 500$  domain. The distribution of the phase field  $\phi$  is the sum of the phase fields  $\phi_i$  with profiles

$$\phi_i(\mathbf{r}) = \frac{1}{2} \left[ 1 - \tanh \left( \frac{\|\mathbf{r} - \mathbf{r}_i\| - r_0}{\sqrt{2}} \right) \right]. \quad (17)$$

from the different seeds  $i$ . Overlaps between different seeds are managed by setting  $\phi = 1$  in all regions where the sums of  $\phi_i > 1$ .<sup>1</sup> After placing initial seeds and adjusting the initial phase field  $\phi$  so that  $\phi \leq 1$  everywhere, the simulation is run up to total time  $t = 200$ , at which time the whole domain is transformed to a solid ( $\phi = 1$ ). This is repeated four times, each time with different random seeds, and the total free energy, time evolution of the solid fraction  $Y$ , discrete particle count  $N$  (the number of disjoint regions with  $\phi = 1$ ) are plotted for the five simulations, and Avrami plots are generated from the five simulations; from the Avrami plot the exponent  $n$  is estimated and compared to the JMAK theory. A snapshot of the phase field at  $t = 40$  is taken for one of the five runs.

Both Problem I.2 and Problem I.3 involve a random number generator. Because different executions will in general generate different random numbers, specific individual solutions

---

<sup>1</sup>Strictly speaking, this may cause  $\phi$  to become non-differentiable at intersection points of the overlapping seeds, however that does not affect numerical convergence when the Laplacian of  $\phi$  is evaluated according to some stencil.

will in general not be reproduced. However, statistics such as the average slope of Avrami plots can be meaningfully compared.

### 3.3. Problem I.3 – Homogeneous nucleation, multiple seeds at random times

For the third part of the homogeneous benchmark problem, the computational domain is first expanded to  $1000 \times 1000$ . Instead of inserting nuclei at fixed time  $t = 0$  as in part two of the problem, in this case 100 random nucleation times are generated,  $t_1, \dots, t_{100}$ , drawn from a uniform distribution in the interval  $t_i \in [0, 600)$  with centers  $\mathbf{r}_i$  drawn from a uniform distribution on the  $1000 \times 1000$  domain. We decrease the driving force to  $\Delta f = \sqrt{2}/12$ , which corresponds to a critical radius of  $r^* = 2$ , but keep the magnitude of initial radii of the inserted nuclei the same as those in the second part of the problem, i.e., Eqs. 17 with  $r_0 = 2.2 = 1.1r^*$ . Again,  $\phi$  is set to unity in regions of overlaps of nuclei. The simulations are run up to times  $t = 600$ , and repeated for four more random initial conditions. The total free energy, the time evolution of the solid fraction  $X$ , and the discrete particle count  $N$  are plotted as functions of time, and an Avrami plot is generated for the five runs. Again, a snapshot of the phase field at  $t = 100$  is taken for one of the five runs.

### 3.4. Problem II – Athermal heterogeneous nucleation

For a benchmark problem on athermal heterogeneous nucleation, a surface with good wetting properties but of limited size is needed. In the usual realistic scenario, these nucleation surfaces represent small, flat, foreign particles which serve as nucleation sites. In order to simplify the problem and to focus it on the athermal nucleation process rather than on technical issues with introducing foreign flat particles, we avoid adding additional boundaries (particles) to the problem formulation, and instead use one of the sides of a rectangular domain by making parts of it a good wetting surface. We use a parameter  $\phi_0$  in Dirichlet boundary conditions on  $\phi$  ( $\phi = \phi_0$ ) to determine the wetting properties of the bounding surface – this corresponds to the “Model B” approach described by Warren *et al* [8]. This “Model B” approach has two advantages: (i) it is very simple to implement, and (ii) if we set  $\phi_0$  large enough, a surface spinodal would occur, i.e., a solid phase will automatically appear at the surface and grow, so we can eliminate the effort of inserting an appropriate seed in the beginning of the simulation. [zero-normal-derivative](#) Neumann boundary conditions ( $\nabla\phi \cdot \hat{\mathbf{n}} = 0$ ) are applied to the other three sides of the computational domain.

The goal of this problem is to explore the behavior around the free growth limit, which, in our 2D setting, is the half-circular configuration of solid on top of a flat surface of length  $2r^*$ , where  $r^*$  is the radius of the homogeneous nucleus corresponding to the given driving force (Eq. 12). To define the problem, the undercooling is set to  $\Delta f_0 = \sqrt{2}/60$ , which corresponds to a critical radius  $r^* = 10$ . We represent the strongly wetting surface of a particle of this size by setting  $\phi_0 = 0.9$  in the  $|x| \leq 10$  inner part, and  $\phi_0 = 0$  in the  $|x| > 10$  outer part of the bottom boundary in a simulation domain of 40 units by 20 units (Fig. 2). Please note that the discontinuities in  $\phi_0$  at  $|x| = 10$  will result in singularities in  $\phi$  around these points with very high local free energy density. This slightly changes the total free energy and the critical undercooling. However, the incurred changes are small enough that they do not change the end result in a discernible way, as whether or not the system passes the free growth limit will depend on the relative energies of configurations near the semi-circular critical configuration. We have, in fact, checked that eliminating these singularities by smearing out the steps in

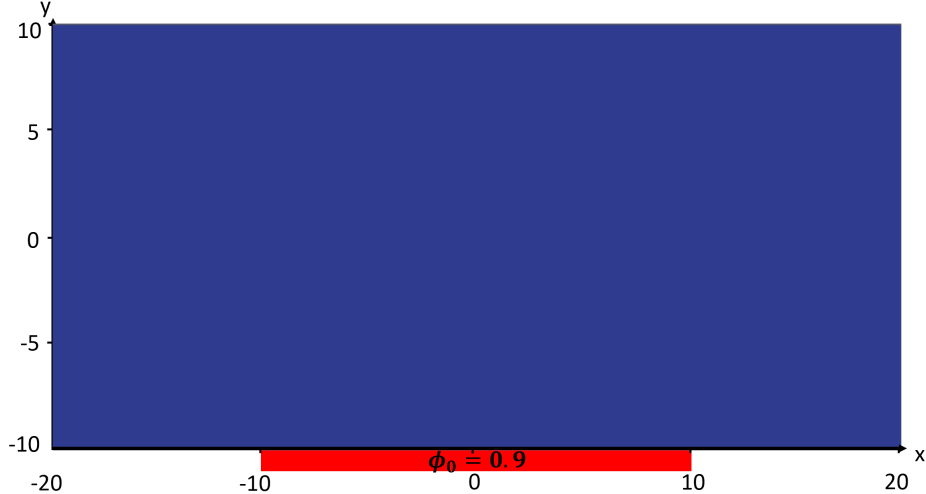


Figure 2: Illustration of the  $40 \times 20$  2D computational domain with Dirichlet boundary conditions on the bottom side and Neumann boundary conditions on the other sides. The red line represents the middle part of the boundary of length 20 where  $\phi_0 = 0.9$ ,  $\phi_0 = 0$  elsewhere.

$\phi_0$  at  $|x| = 10$  in the boundary condition by using tanh profiles slightly increases the critical undercooling by about 1 %. For the purpose of this problem, this difference is acceptable as the aim of the problem formulation is to produce a critical undercooling close to unity which is more easily realizable with a sharp boundary profile than with a diffuse one. Starting from  $\phi = 0$  everywhere in the domain, the simulation is run for times up to  $t = 6500$ , and the transformed fraction  $Y$  is plotted as a function of time  $t$ . The simulation is repeated with the same boundary conditions but varying undercooling  $\Delta f = 0.98\Delta f_0$ ,  $\Delta f = 1.02\Delta f_0$ , and  $\Delta f = 1.04\Delta f_0$ , respectively. We add an additional convergence test with respect to spatial resolution for the solid fraction change when  $\Delta f = 1.1\Delta f_0$  by halving the average linear dimension of the mesh elements until the plots of solid fraction  $Y(t)$  vs. time of two consecutive mesh sizes become indistinguishable.

#### 4. Numerical methods

We use an application within the MOOSE framework [27, 28] for our simulations, as we have done for previous benchmark problems. Solutions obtained with other codes, e.g., FiPy [29] or PRISMS [30], have been uploaded to the PFHub website <https://pages.nist.gov/pfhub/> [24].

The computational domains created by the MOOSE application are meshed using square, four-node quadrilateral elements. First-order Lagrange shape functions are employed for the order parameter  $\phi$ . The system of nonlinear equations is solved with the full Newton method that uses the single-matrix preconditioning with the additive Schwarz preconditioner and ILU sub-preconditioning. The second backward differentiation formula (BDF2) time integration scheme is applied. The simulations are solved with a nonlinear relative tolerance of  $10^{-6}$  and a nonlinear absolute tolerance of  $10^{-9}$ . A maximum of ten nonlinear iterations per solve, and a maximum of 50 linear iterations, are specified. To improve computational efficiency,

adaptive meshing and adaptive time stepping are used. The initial time step  $\Delta t$  is set to 0.01, and the time step is allowed to grow by 5 % per step. For Problem I.3, if  $\Delta t$  grows too large then many nucleation events may occur in one time step. In order to reduce the probability of this and force nucleation events to occur at different times,  $\Delta t$  is capped at unity and is also reduced to 0.1 if a nucleus has just been added to the system, from which  $\Delta t$  is allowed to grow again. In addition, this scheme can also help with the convergence of solvers. For the single-seed homogeneous nucleation part of the first problem, the mesh contains  $64 \times 64$  elements. This translates to an element size of  $\Delta x = 1.5625$ . A single element can be refined up to four times for adaptive meshing. Thus the finest part of the mesh has elements with size  $\Delta x = 0.09765$ . The convergence test for the solid fraction change in the  $r_0 = 1.01r^*$  case is done by four simulations with different fixed spatial resolutions ( $\Delta x = 0.8, 0.4, 0.2, 0.1$ ), and compared with applying the adaptive mesh. For the second and third parts of the first problem, the mesh contains  $160 \times 160$ , and  $320 \times 320$  elements, respectively, which result in the same spatial resolution,  $\Delta x = 3.125$ , and the finest part of the mesh has elements with size  $\Delta x = 0.1953$ . For the second problem, on athermal nucleation, the mesh contains  $100 \times 50$  elements, which gives an element size of  $\Delta x = 0.4$ . With the adaptive meshing, the size of the smallest element is  $\Delta x = 0.025$ . Five different spatial resolutions ( $\Delta x = 0.4, 0.2, 0.1, 0.05, 0.025$ ) are used for the convergence test when plotting the solid fraction versus time for the  $\Delta f = 1.1\Delta f_0$  case. We also compare the results with the simulation using adaptive meshing.

## 5. Results and discussion

In this section, we discuss the example solutions and metrics obtained from them. We also study error and convergence behavior for the  $r_0 = 1.01r^*$  case in the single seed homogeneous nucleation problem and the  $\Delta f = 1.1\Delta f_0$  case in the athermal heterogeneous nucleation problem. Furthermore, we discuss some peculiar issues that may arise in solving these benchmark problems.

### 5.1. Problem I.1 – Homogeneous nucleation, single seed

For this problem we mainly look into how the initial radius of the inserted seed determines whether the nucleation is going to happen or not. We choose the total free energy of the system and the solid fraction as metrics with which to compare simulation results.

Fig. 3 shows the total free energy of the system, and Fig. 4 shows how the solid fraction changes over time. When the initial radius of the seed is smaller than the critical radius, e.g.,  $r_0 = 0.99r^*$ , based on classical nucleation theory, the quantity  $d\Delta G/dr$  in Eq. 9 is positive. That means that it is energetically more favorable for the system to decrease the size of the nucleus. As a result, the total free energy (black dashed line in Fig. 3) and the solid fraction (black dashed line in Fig. 4) both decrease over time. The inserted seed shrinks and at  $t \approx 90$ , it fully dissolves into the liquid. The solid fraction drops to zero and the total free energy of the system stops decreasing. Nucleation does not happen in this case. On the other hand, when the initial radius of the seed is larger than the critical radius ( $r_0 = 1.01r^*$ ),  $d\Delta G/dr$  in Eq. 9 is negative, and it is energetically favorable for the system to increase the size of the nucleus, i.e., the system lowers its free energy by growing the solid fraction from

the inserted seed. We note that with no fluxes entering or leaving the system, the total energy is necessarily monotonically non-increasing.

When the initial radius of the seed is equal to the critical radius ( $r_0 = 1.00r^*$ ),  $d\Delta G/dr$  in Eq. 9 is equal to zero, and the system is in an unstable equilibrium state. Therefore, the total free energy (red solid line in Fig. 3) stays approximately constant. Ideally, the solid fraction would also remain constant. The small changes in the calculated solid fraction (red solid line in Fig. 4) when  $t$  is large are due to numerical errors that accumulate with time. Because the system is unstable, small errors will then eventually lead to growth or shrinkage of the nucleus.

The convergence test for the solid fraction change for the case  $r_0 = 1.01r^*$  is shown in Fig. 5. We use an  $L^2$  metric as convergence check. The  $L^2$  error,  $e_{L^2}$ , between two consecutive runs  $i - 1$  and  $i$  is defined as

$$e_{L^2} = \int |\phi_i(\mathbf{r}, t = 200) - \phi_{i-1}(\mathbf{r}, t = 200)|^2 d\mathbf{r}. \quad (18)$$

The ability to calculate the  $L^2$  error involves interpolating solutions to different meshes. Because this can be a bit challenging technically, we did not explicitly include calculating the  $L^2$  error in the problem definition. We choose  $r_0 = 1.01r^*$  for the convergence test because the system is very sensitive when  $r_0 = 1.00r^*$ , and small numerical errors can result in exponential growth of error. On the other hand, if  $r_0$  is far enough away from  $r^*$ , numerical integration is rather robust and convergence is readily achieved. Figure 5 clearly shows that the mesh resolution has a significant effect on the time-evolution of the solid fraction. When the mesh is of low resolution, i.e.,  $\Delta x = 0.8$ , only a small increase in solid fraction is observed before  $t = 200$ , and the nucleus grows slowly. When we refine the mesh to improve the spatial resolution, the solid fraction increases more rapidly. The calculated  $L^2$  error between simulations with consecutive meshes  $\Delta x = 0.4$  and  $\Delta x = 0.2$  is 2.78, and that between mesh sizes of  $\Delta x = 0.2$  and  $\Delta x = 0.1$  is 0.69, which indicates that the results from the latter pair of meshes are similar. Further increases in the mesh resolution would not significantly improve the accuracy of the simulation results. This is also indicated in Fig. 5 where the curves of  $\Delta x = 0.2$  and  $\Delta x = 0.1$  are indistinguishable. The adaptive mesh behaves similarly to the refined fixed mesh. We thus treat the solution generated with  $\Delta x = 0.1$  as a gold standard solution for comparison with the results of other numerical solution methods and implementations.

## 5.2. Problem I.2 – Homogeneous nucleation, multiple seeds at $t = 0$

For this part of the homogeneous nucleation benchmark problem we mainly look into the nucleation behavior when multiple seeds are inserted at  $t = 0$ . Besides the total free energy of the system and the solid fraction, we also add the number of discrete particles (calculated by using FeatureFloodCount postprocessor in MOOSE) and the Avrami plot as metrics to

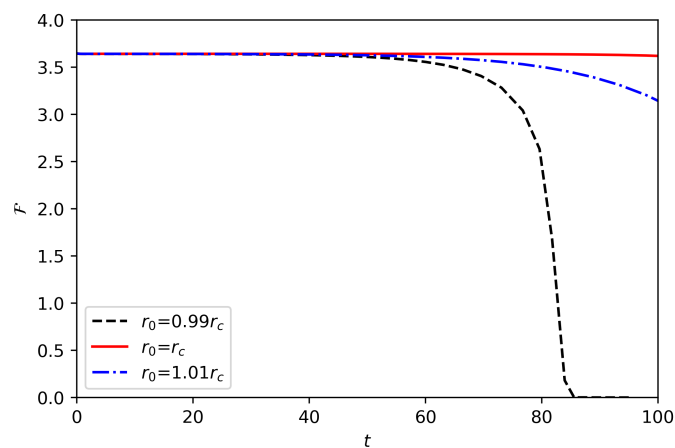


Figure 3: The total free energy evolution of the single seed homogeneous nucleation.

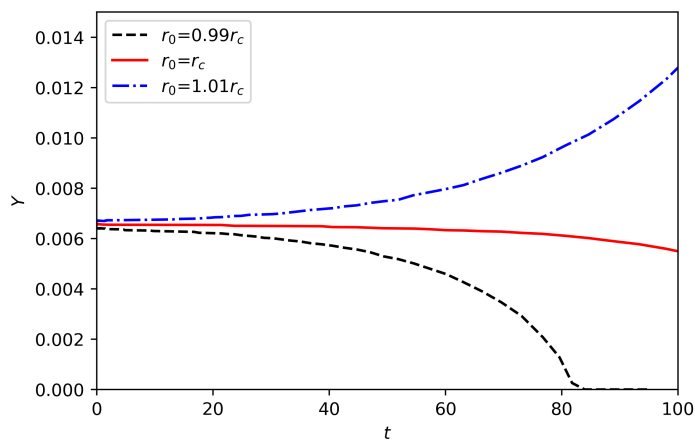


Figure 4: The solid fraction of the single seed homogeneous nucleation.

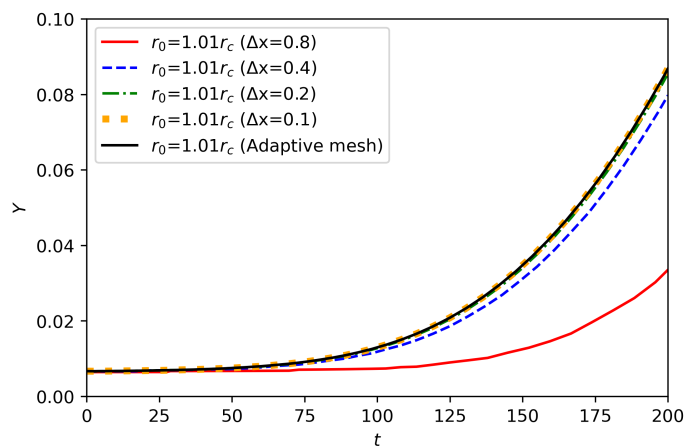


Figure 5: Convergence test for the solid fraction change for  $r_0 = 1.01r^*$ .

illustrate the transformation kinetics. Figures 6, 7, 8, 9 depict the calculated total free energy of the system, solid fraction, number of discrete particles, and the Avrami plot for the multiple-seed homogeneous nucleation that happens at  $t = 0$ , respectively. Different colors in the figures represent runs with different random seeds. A snapshot of the phase field domain at  $t = 40$  is taken and shown in Fig. 10.

In all five cases with different random nuclei positions, the total free energy is decreasing monotonically, as shown in Fig. 6, as should be the case. Since the initial radius for the nuclei is larger than the critical radius, we expect to see an increase for the solid fraction over time, and the nuclei should grow and eventually fill up the entire simulation volume. This is indeed the case, as shown in Fig. 7. The solid fraction increases with time in an S-shaped curve with a short left tail. The short tail means that the early stage of nucleation with a low transformation rate is short, since all the nuclei are inserted and ready to grow at time  $t = 0$ . For most cases, the number of discrete particles starts at 25 since we insert 25 seeds at  $t = 0$ . However, the number of discrete particles can be smaller, e.g., 24 or even less, if two or more inserted seeds overlap. The number of discrete particles also decreases monotonically and finally drops to unity at some time between  $t = 75$  and 100, which indicates that the nuclei have merged into one large particle. The snapshot in Fig. 10 is used as an illustration, showing twelve discrete particles at  $t = 40$  which is the outcome of particles merging. Notice that the seeds in Fig. 10 have equal size since they are inserted at the same time  $t = 0$ . The nucleation kinetics is compared with the JMAK theory by making the Avrami plots in Fig. 9 and extracting the exponent  $n$ . Note that we could also fit the solid fraction  $Y(t)$  directly to the functional form given by the JMAK theory,  $Y(t) = 1 - \exp[-Kt^n]$ . Extracting the power  $n$  in JMAK theory from the Avrami plots vs. direct fit to the functional form tends to give slightly different results as different points are weighted differently, and the Avrami plots tend to enhance the error in the early and late stages of the transformation. However, it is more common to use the Avrami plots in experiments to obtain the kinetic coefficient; therefore, we use the Avrami plots here.

When all the nucleation events happen at  $t = 0$ , the slope of the Avrami plot should be close to the dimension of the simulation domain, which is 2 in this case. Ideally the size of the system should be infinite for the JMAK theory to hold, but this is not realistic in our simulation. We fit a straight line to the data ranging from  $1.1 < \log t < 2.1$ . The average slope of the fitted line for the five runs is  $\langle n \rangle = 2.01$ , and the standard deviation is 0.0376. In addition, we see that the Avrami plots of the five runs with different initial random positions overlap with each other very well. This indicates that the initial positions of the nuclei have little influence on the nucleation kinetics.

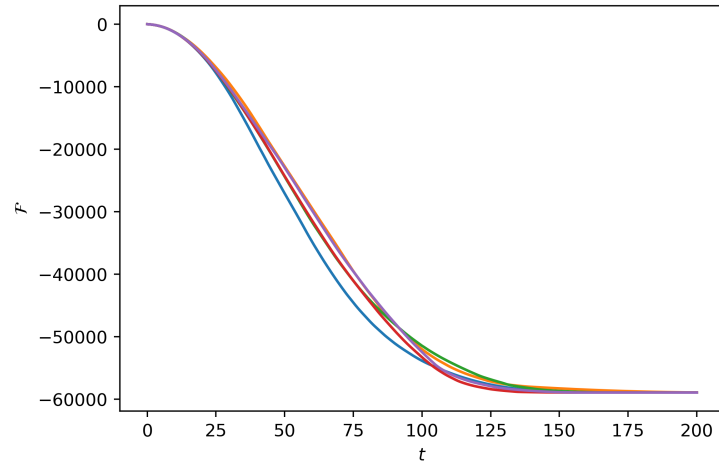


Figure 6: The total free energy evolution of the multiple seed homogeneous nucleation with all seeds nucleating at  $t = 0$ .

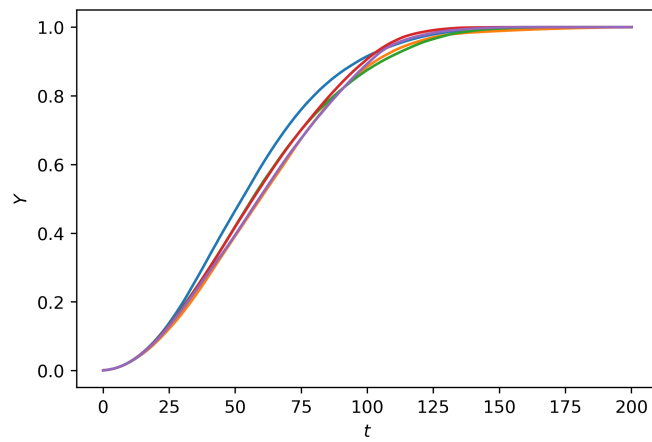


Figure 7: The solid fraction of the multiple seed homogeneous nucleation with all seeds nucleating at  $t = 0$ .

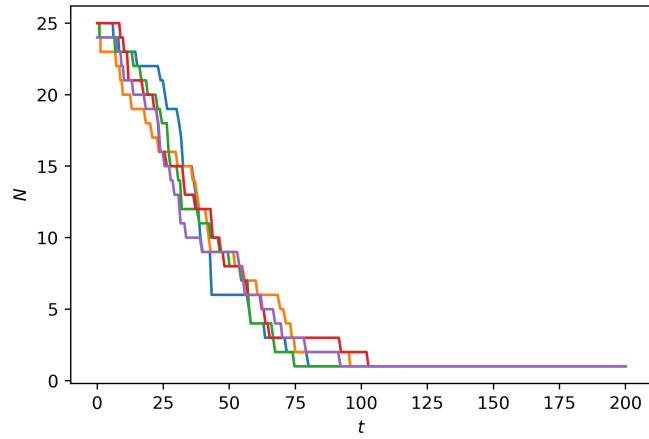


Figure 8: The number of discrete particles of the multiple seed homogeneous nucleation with all seeds nucleating at  $t = 0$ .

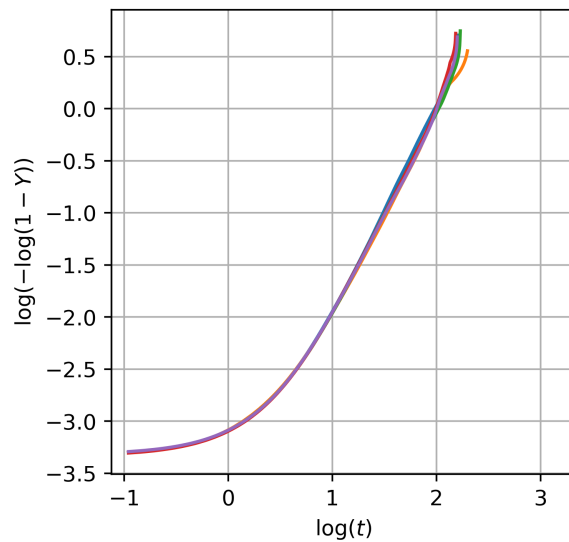


Figure 9: The Avrami plots of the multiple seed homogeneous nucleation with all seeds nucleating at  $t = 0$ . The average slope fitted within the range of  $1.1 < \log t < 2.1$  is 2.01, and the standard deviation is 0.0376.

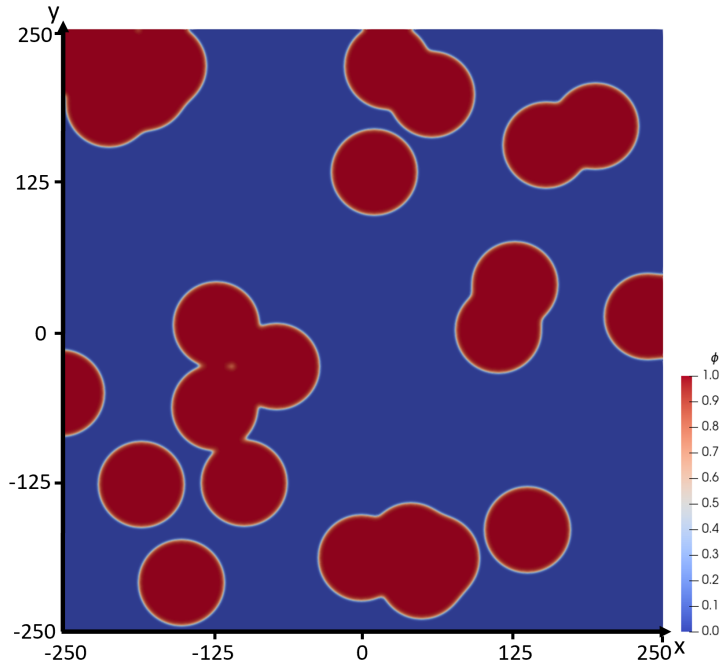


Figure 10: The phase field domain of  $\phi$  at  $t = 40$  of the multiple seed homogeneous nucleation with all seeds nucleating at  $t = 0$ .

### 5.3. Problem I.3 – Homogeneous nucleation, multiple seeds at random times

For this part of the homogeneous nucleation benchmark problem we examine the nucleation behavior when multiple seeds are inserted at random times. We use the same metrics as in the previous problem, (Fig. 11, 12, 13, and 14) with also a snapshot of the phase field domain at  $t = 100$  as shown in Fig. 15. Just as in Problem I.2, different colors in the figures represent runs with different random seeds.

Compared to what we observed for homogeneous nucleation with multiple seeds at the same time, the total free energy curve shows a similar decreasing trend but it is now not necessarily monotonic. This is because every time we insert a nucleus there is an increase in the total free energy. However, this energy increase is so small, about four orders of magnitude less than the total energy change in the entire time range, so one cannot really notice corresponding glitches in the energy plot. The solid fraction increases monotonically. The main difference is related to the shape change of the solid-fraction curve. Transformations are observed to follow a characteristic sigmoidal profile (as shown in Fig. 12), where the transformation rates are low at the beginning and the end of the transformation but rapid in between. (In contrast, for homogeneous nucleation with multiple seeds at  $t = 0$ , the Avrami plots are approximately straight lines after the initial slow growth, Fig. 9.) The initial slow rate can be attributed to the time required for forming a significant number of nuclei of the solid phase.<sup>2</sup> During the intermediate period the transformation is rapid as the nuclei grow into particles and consume the old liquid phase while nuclei continue to form in the

<sup>2</sup>The initial near-vertical lines for a few of the plots is an artifact of an aggressive adaptive time stepper: if the time step has grown too large before the initial seed is inserted, the code does not tag the insertion time accurately and the growth between the first and second time step after insertion is inaccurate.

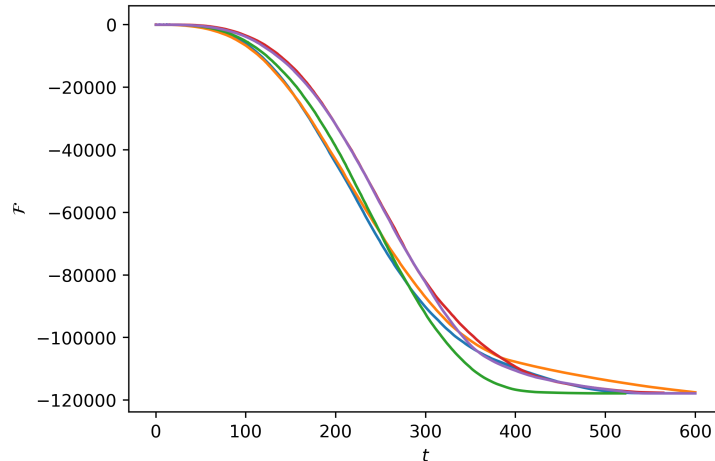


Figure 11: The total free energy evolution of the multiple seed homogeneous nucleation with seed nucleating at random times.

remaining liquid phase. Once the transformation nears completion the liquid phase in the domain has almost all been consumed: there is not much space left for nuclei to form and the production of new particles slows down. Furthermore, the particles already existing begin to overlap, forming a boundary where growth of solid phase stops. Figure 15 is an example showing the growth of the particles at  $t = 100$ . Notice that in contrast with the snapshot shown in Fig. 10, this time the particles have different sizes since the seeds are inserted at different times. The number of discrete particles is 0 at  $t = 0$ . As the time increases up to around  $t = 200$ , more new nuclei are added to the system at rate that outpaces nuclei merging events, resulting in an overall increase in the number of discrete particles. After that, the merging rate is greater than the insertion rate. Therefore, the number of discrete particles starts to decrease and finally drops to unity as in the homogeneous nucleation with seeds at  $t = 0$ . For a quantitative comparison of the nucleation kinetics, we calculate the slope of the Avrami plots. This time when nucleation happens at different random times, and the slope of the Avrami plots should be around 3.0, according the JMAK theory (two dimensions of growth plus one, a constant growth rate). We fit a straight line to the data ranging from  $1.5 < \log t < 2.5$ . The average slope of the fitted line for the five runs is  $\langle n \rangle = 3.07$ , and the standard deviation is 0.180. Although the Avrami plots of the five runs with different initial random positions do not overlap as well as for the case with all seeds at  $t = 0$ , the average slope is close to the ideal value 3.0 and the variance is small. This again indicates that the nucleation kinetics do not depend on the choice of the pseudorandomly generated seed.

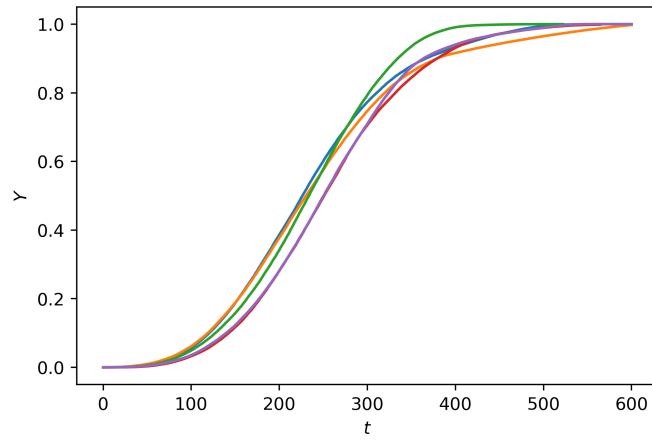


Figure 12: The solid fraction of the multiple seed homogeneous nucleation with seed nucleating at random times.

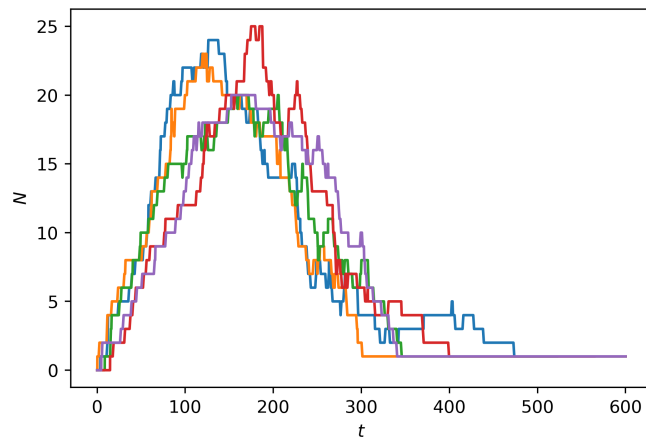


Figure 13: The number of discrete particles of the multiple seed homogeneous nucleation with seed nucleating at random times.

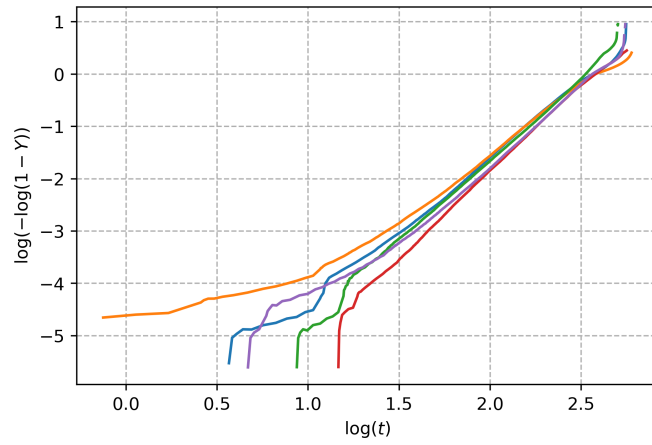


Figure 14: The Avrami plots of the multiple seed homogeneous nucleation with seed nucleating at random times. The average slope fitted within the range of  $1.5 < \log t < 2.5$  is 3.07, and the standard deviation is 0.180.

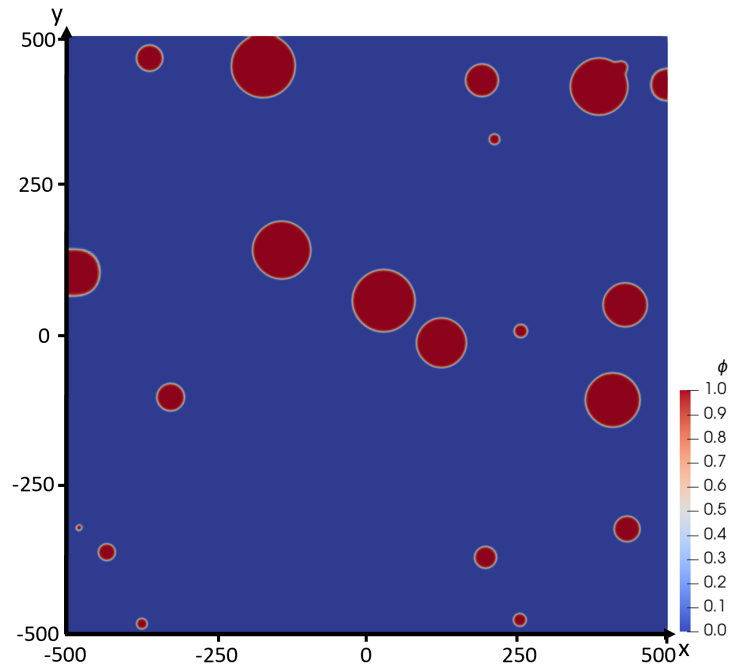


Figure 15: The phase field domain of  $\phi$  at  $t = 100$  of the multiple seed homogeneous nucleation with seed nucleating at random times.

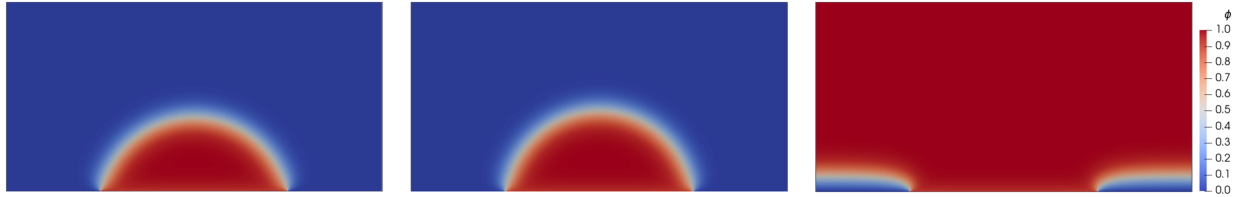


Figure 16: The snapshot for the athermal heterogeneous nucleation at  $t = 6500$  when (a)  $\Delta f = 0.98\Delta f_0$ , (b)  $\Delta f = 1.00\Delta f_0$ , (c)  $\Delta f = 1.02\Delta f_0$ .

#### 5.4. Problem II – Athermal heterogeneous nucleation

In this benchmark problem we study how the driving force for solidification influences the free-growth condition of athermal heterogeneous nucleation. Figure 16 shows what the system looks like at  $t = 6500$  under different driving forces.

When the applied undercooling driving force  $\Delta f = 1.00\Delta f_0$ , the particle will reach its free growth limit, which is the half-circular configuration, and its radius is equal to the radius of the homogeneous nucleus corresponding to the given driving force. When  $\Delta f = 0.98\Delta f_0$ , the corresponding critical radius increases, the newly formed nucleus on the surface cannot grow freely, its final shape could be treated as part of a circle with larger radius compared to the previous case. The solid fraction of these two cases increases at the beginning but would reach a plateau very soon (black solid line and red dashed line in Fig. 17). When we increase the undercooling driving force to  $\Delta f = 1.02\Delta f_0$ , the corresponding critical radius decreases, the particle is able to grow freely and almost takes up the space of the entire system. The corresponding solid fraction would keep increasing until it becomes close to 1. We remark that the system is very sensitive to numerical errors around  $\Delta f = 1.00\Delta f_0$ ; for some methods, free growth cannot be observed when  $\Delta f = 1.02\Delta f_0$ . Further increasing the driving force to  $\Delta f = 1.04\Delta f_0$  may help the free growth to occur. Unsurprisingly, for those methods that evidenced free growth at  $\Delta f = 1.02\Delta f_0$ , a faster growth rate is observed when  $\Delta f = 1.04\Delta f_0$ .

We have performed a convergence test for the solid fraction change for an undercooling driving force of  $\Delta f = 1.1\Delta f_0$ , as shown in Fig. 18. As we refined the mesh resolution from  $\Delta x = 0.4$  to  $\Delta x = 0.025$ , the solid fraction curve would gradually shift to the right – with decreasing element size, it takes longer for the free growth to occur. Our  $L^2$  error at  $t = 800$  is 0.42 between mesh sizes of  $\Delta x = 0.05$  and  $\Delta x = 0.025$ , the  $L^2$  error is 0.23 between mesh sizes of  $\Delta x = 0.025$  and  $\Delta x = 0.0125$ . Figure 18 shows that visually, the difference between mesh size of  $\Delta x = 0.05$  and  $\Delta x = 0.025$  is already barely discernible. It is interesting to note that the result for a mesh size of  $\Delta x = 0.0125$  (not shown) is indistinguishable from using adaptive meshing – and at least in our case the run-time for adaptive meshing was smaller by orders of magnitudes than the run-time for a fixed mesh with  $\Delta x = 0.0125$ . Please note that the undercooling  $\Delta f = 1.1\Delta f_0$  is safely above the critical undercooling, shown by the fact that the transition happens rapidly, without any initial period of slow growth or “hesitation”. As the system approaches the critical undercooling, the system becomes more sensitive to small details, such as the solver type and the numerical resolution used; therefore, one should expect slower or worse convergence and also reduced reproducibility between solvers when closer to the critical value.

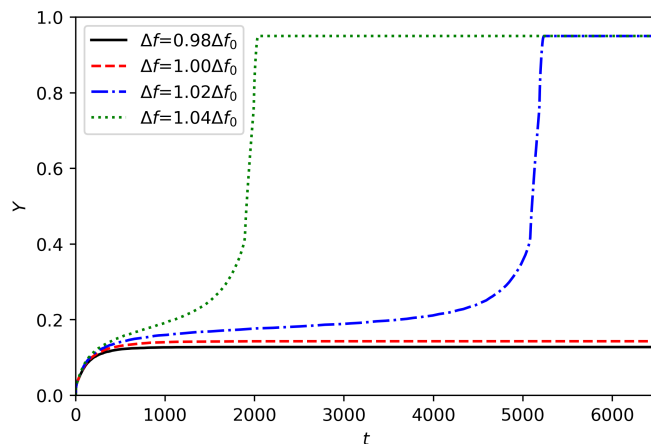


Figure 17: The solid fraction of the athermal heterogeneous nucleation for  $\Delta f = 0.98\Delta f_0$ ,  $\Delta f = 1.00\Delta f_0$ ,  $\Delta f = 1.02\Delta f_0$ , and  $\Delta f = 1.04\Delta f_0$ .

## 6. Conclusion

The benchmark problems on homogeneous and heterogeneous nucleation presented in this work are an addition to our ongoing work to develop benchmark problems for phase field modeling [1, 2, 3]. It is our hope that the discussions of these problems are of instructional value to practitioners, teachers, and students. On a pedagogical level, the first nucleation problem illustrates that an initial particle will shrink and dissolve when its initial radius is smaller than the critical radius, and that it will grow when its initial radius is larger than the critical radius. The second and third parts of this problem provide simple illustrations of nucleation kinetics and connect the results to the JMAK theory. When the nucleation happens at  $t = 0$ , the slope of the Avrami plot is approximately equal to  $d$ , where  $d$  is the domain dimension. When the nucleation happens at random times, the slope of the Avrami plot is approximately  $d + 1$ . The second problem demonstrates the free growth condition for the athermal heterogeneous nucleation. Free growth will only occur when the driving force of solidification is larger than the critical driving force corresponding to the critical radius.

As benchmark problems are aimed at probing numerical implementations, the problems highlight several potential issues. Numerical solutions are sensitive to any perturbations or numerical noise when initial radii are close to the critical radius  $r^*$ . This is evident in Problem I.1 (single-seed nucleation). Depending on the numerical implementation and the specific code, the solid fraction at an initial radius  $r_0 = r^*$  could either increase or diminish (Fig. 4). Similarly, for the athermal nucleation (Problem II), different numerical implementations and codes may give different results close to critical driving force (Fig. 17), with the steep onset of growth occurring at later or earlier times.

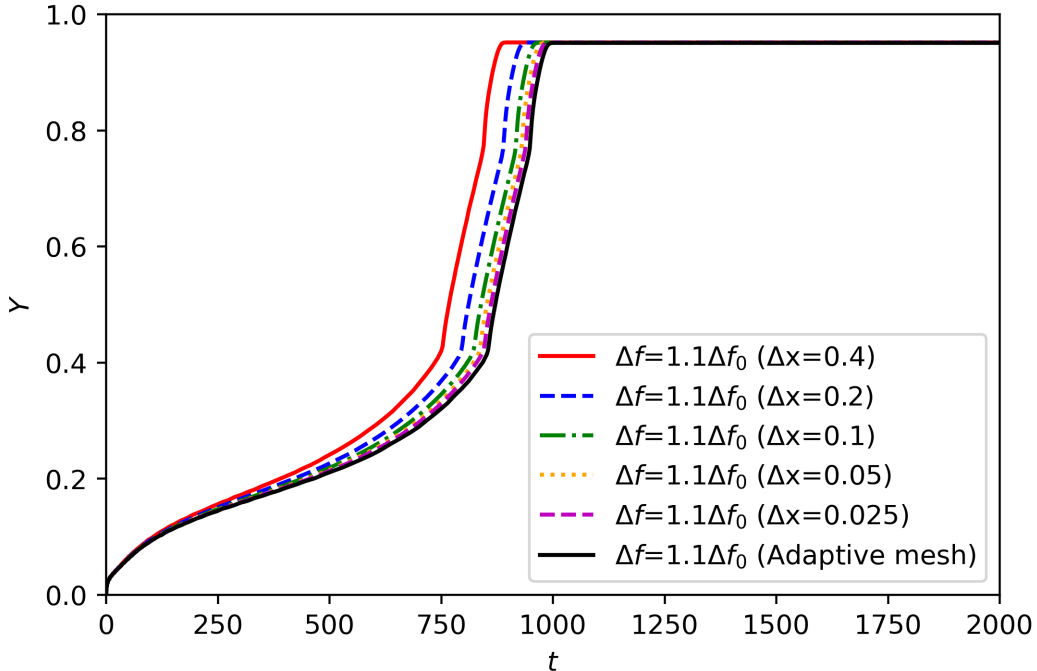


Figure 18: The convergence test for the solid fraction change in the case  $\Delta f = 1.1\Delta f_0$ .

A related issue is that when  $r_0$  is close to  $r^*$  in single-seed homogeneous nucleation, or close to critical driving force in single-seed athermal nucleation, the convergence with respect to mesh size can be slow and care has to be taken to ensure that the results are well converged with respect to mesh size. This is especially the case for the athermal nucleation close to critical driving force ( $\Delta f = 1.1f_0$ ), where we had to reduce the mesh size to  $\Delta x = 0.025$  for well-converged solution. It is interesting – and reassuring – to note that in both cases, adaptive meshing led to well-converged solutions at much smaller execution time than for a fine uniform mesh. This clearly demonstrates the power of adaptive meshing schemes for these problems.

The slopes of the Avrami plots, especially for multiple seeds at  $t = 0$ , are usually found to be larger than the ideal value  $d$ . The reason for this is subtle: the JMAK model assumes circular particles, sometimes overlapping. At the points of overlap, there will be cusps in the boundary of the merged particles (see, e.g., Fig. 10). Because the Cahn-Hilliard equations correctly incorporate the Gibbs-Thomson effect, the time-evolution of the systems seeks to smooth out cusps and make them straighter. This leads to a faster growth of the solid fraction than predicted by the JMAK theory. This is particularly evident at smaller driving forces where contributions to the free energy from the Gibbs-Thomson effect are relatively larger. We initially ran simulations for Problem I.2 (multiple seeds at  $t = 0$ ) with a driving force  $\Delta f = \sqrt{2}/12$ . This resulted in slopes in the Avrami plots of close to 2.3. Increasing the driving force by a factor of 2 to  $\Delta f = \sqrt{2}/6$  has the effect of decreasing the interfacial energy contribution relative to the bulk free energy, which diminishes the Gibbs-Thomson effect and slows down the growth of the solid fraction so the slope in the Avrami plot approaches the

ideal value. We confirmed that for the system sizes used here ( $500 \times 500$ ), the slopes in the Avrami plots were not affected by finite-size effects. On the other hand, Problem I.3 (multiple seeds at random times) gave slopes very close to the ideal value of  $d + 1$  without increasing the driving force from  $\Delta f = \sqrt{2}/12$ . We believe this is because the constant-rate nucleation yields a better average over microscopic processes thereby diminishing the effect of cusps.

The development of these benchmark problems, as the ones before them, has relied very heavily on comments and feedback from the community. It is a great experience to work in this way with an enthusiastic and engaged community. In order to make these benchmark problems as useful as possible, we urge the community to continue to provide feedback for existing and possible additional benchmark problems at <https://pages.nist.gov/pfhub/>, and to implement these benchmark problems and upload completed results.

## Acknowledgments

This work was performed under financial assistance award 70NANB19H005 from the U.S. Department of Commerce, National Institute of Standards and Technology as part of the Center for Hierarchical Material Design (CHiMaD). DM was supported by the U.S. Department of Energy, Office of Basic Energy Sciences, Division of Materials Sciences and Engineering under Award #DE-SC0008637 as part of the Center for Predictive Integrated Structural Materials Science (PRISMS Center) at University of Michigan. TP and LG were supported by the National Agency for Research, Development, and Innovation, Hungary (NKFIH contract no. KKP-126749). We gratefully acknowledge the computing resources provided on Bebop and Blues, high-performance computing clusters operated by the Laboratory Computing Resource Center at Argonne National Laboratory. We particularly thank the participants of the Phase Field Workshops held in Evanston, IL, to whom we are deeply indebted for invaluable feedback and comments. We also thank Dr. T. Keller (NIST) and Dr. M. Donahue for helpful and insightful comments.

## References

- [1] A. M. Jokisaari, P. W. Voorhees, J. E. Guyer, J. A. Warren, O. G. Heinonen, Benchmark problems for numerical implementations of phase field models, *Computational Materials Science* 126 (2017) 139–151.
- [2] A. M. Jokisaari, P. W. Voorhees, J. E. Guyer, J. A. Warren, O. G. Heinonen, Phase field benchmark problems for dendritic growth and linear elasticity, *Computational Materials Science* 149 (2018) 336–347.
- [3] A. M. Jokisaari, W. Wu, P. W. Voorhees, J. E. Guyer, J. A. Warren, O. G. Heinonen, Phase field benchmark problems targeting fluid flow and electrochemistry, *Computational Materials Science* 176 (2020) 109548.
- [4] L. Gránásy, , T. Börzsönyi, T. Pusztai, Nucleation and bulk crystallization in binary phase field theory, *Physical Review Letters* 88 (2002) 206105.

- [5] M. Castro, Phase-field approach to heterogeneous nucleation, *Physical Review B* 67 (2003) 035412.
- [6] J. P. Simmons, Y. Wen, C. Shen, Y. Wang, Microstructural development involving nucleation and growth phenomena simulated with the phase field method, *Materials Science and Engineering: A* 365 (2004) 136–143.
- [7] L. Gránásy, T. Pusztai, D. Saylor, J. A. Warren, Phase field theory of heterogeneous crystal nucleation, *Physical Review Letters* 98 (2007) 035703.
- [8] J. A. Warren, T. Pusztai, L. Környei, L. Gránásy, Phase field approach to heterogeneous crystal nucleation in alloys, *Physical Reviews B* 79 (2009) 014204.
- [9] T. W. Heo, L. Chen, Phase-field modeling of nucleation in solid-state phase transformations, *The journal of the minerals, metals & materials society* 66 (2014) 1520–1528.
- [10] L. Gránásy, G. Tóth, J. A. Warren, F. Podmaniczky, G. Tegze, L. Rátkai, T. Pusztai, Phase-field modeling of crystal nucleation in undercooled liquids – a review, *Progress in Materials Science* 106 (2019) 100569.
- [11] R. Kubo, The fluctuation-dissipation theorem, *Reports on Progress in Physics* 29 (1966) 255–284.
- [12] J. P. Simmons, C. Shen, Y. Wang, Phase field modeling of simultaneous nucleation and growth by explicitly incorporating nucleation events, *Scripta Materialia* 43 (2000) 935–942.
- [13] R. Shi, S. Khairallah, T. W. Heo, M. Rolchigo, J. T. McKeown, M. J. Matthews, Integrated simulation framework for additively manufactured Ti-6Al-4V: melt pool dynamics, microstructure, solid-state phase transformation, and microelastic response, *The Journal of The Minerals, Metals & Materials Society* 71 (2019) 3640–3655.
- [14] W. A. Johnson, R. F. Mehl, Reaction kinetics in processes of nucleation and growth, *Am. Inst. Min. Metal. Petro. Eng.* 135 (1939) 416–458.
- [15] M. Avrami, Kinetics of phase change. I General theory, *The Journal of Chemical Physics* 7 (1939) 1103–1112.
- [16] M. Avrami, Kinetics of phase change. II Transformation-time relations for random distribution of nuclei, *The Journal of Chemical Physics* 8 (1940) 212–224.
- [17] M. Avrami, Granulation, phase change, and microstructure kinetics of phase change. III, *The Journal of Chemical Physics* 9 (1941) 177–184.
- [18] A. N. Kolmogorov, On the statistical theory of the crystallization of metals, *Bulletin of the Academy of Sciences of the USSR* 1 (1937) 355–359.
- [19] T. E. Quested, A. L. Greer, Athermal heterogeneous nucleation of solidification, *Acta Materialia* 53 (2005) 2683–2692.

- [20] A. L. Greer, A. M. Bunn, A. Tronche, P. V. Evans, D. J. Bristow, Modelling of inoculation of metallic melts: application to grain refinement of aluminium by Al–Ti–B, *Acta materialia* 48 (2000) 2823–2835.
- [21] A. L. Greer, Overview: Application of heterogeneous nucleation in grain-refining of metals, *The Journal of Chemical Physics* 145 (2016) 211704.
- [22] R. Shi, C. Shen, S. A. Dregia, Y. Wang, Form of critical nuclei at homo-phase boundaries, *Scripta Materialia* 146 (2018) 276–280.
- [23] L. Zhang, L.-Q. Chen, Q. Du, Morphology of critical nuclei in solid-state phase transformations, *Physical Review Letters* 98 (2007) 265703.
- [24] D. Wheeler, T. Keller, S. J. DeWitt, A. M. Jokisaari, D. Schwen, J. E. Guyer, L. K. Aagesen, O. G. Heinonen, M. R. Tonks, P. W. Voorhees, et al., PFhub: The phase-field community hub, *Journal of Open Research Software* 7 (2019).
- [25] S. M. Allen, J. W. Cahn, A microscopic theory for antiphase boundary motion and its application to antiphase domain coarsening, *Acta Metallurgica* 27 (1979) 1085–1095.
- [26] C. Shen, J. Li, Y. Wang, Finding critical nucleus in solid-state transformations, *Metallurgical and Materials Transactions A* 39 (2008) 976–983.
- [27] D. Gaston, J. Peterson, C. Permann, D. Andrs, A. Slaughter, J. Miller, Continuous integration for concurrent computational framework and application development, *Journal of Open Research Software* 2 (2014).
- [28] D. R. Gaston, C. J. Permann, J. W. Peterson, A. E. Slaughter, D. Andrš, Y. Wang, M. P. Short, D. M. Perez, M. R. Tonks, J. Ortensi, et al., Physics-based multiscale coupling for full core nuclear reactor simulation, *Annals of Nuclear Energy* 84 (2015) 45–54.
- [29] J. E. Guyer, D. Wheeler, J. A. Warren, FiPy: Partial differential equations with Python, *Computing in Science & Engineering* 11 (2009) 6–15.
- [30] S. DeWitt, S. Rudraraju, D. Montiel, W. B. Andrews, K. Thornton, PRISMS-PF: A general framework for phase-field modeling with a matrix-free finite element method, *npj Computational Materials* 6 (2020) 1–12.